Stabilized two-phase material point method for hydromechanical coupling problems in solid-fluid porous media

Xiong Tang[1, 2, 3], Wei Liu[1, 2], Siming He[1, 2], Lei Zhu[1, 2], Michel Jaboyedoff[3], Huanhuan Zhang[1, 2], Yuqing Sun[1, 2], Zenan Huo[3]

[1] Institute of Mountain Hazards and Environment, Chinese Academy of Sciences, Chengdu 610041, China

[2] University of Chinese Academy of Sciences, Beijing 100049, China

[3] Analysis Group, Institute of Earth Sciences, University of Lausanne, CH 1015 Lausanne, Switzerland

Correspondence: Wei Liu (spon@imde.ac.cn), Siming He (hsm@imde.ac.cn)

Abstract. For the hydromechanically coupling of solid-fluid porous media, this study presents an explicit stabilized two-phase material point method (MPM) formulation based on the one-point two-phase MPM scheme. To mitigate the spurious pore pressure and maintain the numerical stability, the stabilized techniques including the strain smoothing method and the multi-field variational principle are implemented in the proposed formulation. The strain smoothing technique is used to smooth the volumetric strain rate, and the calculation of the pore pressure increment at particles is based on the multi-field variational principle. Four numerical examples are performed to evaluate the performance of the proposed formulation. With its effective and easy-to-implement stabilized techniques, the proposed formulation provides stable and reliable outcomes that align well with analytical solutions and results from other approaches, offering extensive validation that the proposed two phase MPM formulation is an effective and reliable approach for the simulation of solid-fluid porous media under both static and dynamic conditions.

1 Introduction

The hydromechanically coupling of solid-fluid porous media widely presents in

nature and engineering, from natural processes like rainfall-induced landslide and earthquake-induced liquefaction, to coastal dike-breaking and offshore foundations (Jerolmack and Daniels, 2019; Zhan et al., 2025; Guan and Shi, 2023). Due to the practical importance, reproducing and understanding the physical nature of such a two-phase system have attracted strong research interests across many scientific and engineering disciplines, which has become increasingly recognized with recent advances in both observational and simulation tools (Li et al., 2023; Taylor-Noonan et al., 2022; Pudasaini and Mergili, 2019). Numerical modeling of this two-phase coupling system is of great interest in geological hazard prevention and geotechnical field, yet it remains a significant challenge for researchers in many disciplines alike.

In soil-fluid coupling problems, the motion of each constituent is governed by stress distributions, external gravity forces and interaction forces (Pudasaini and Mergili, 2019; Baumgarten and Kamrin, 2018; Bandara and Soga, 2015). For the simulation of this two-phase system, various numerical methods have been proposed, including the smoothed particle hydrodynamics (SPH) method (Lian et al., 2023; Chen et al., 2023), the particle finite element method (Yuan et al., 2022; Jin and Yin, 2022), and the material point method (MPM) (Bandara and Soga, 2015; Bandara et al., 2016; Jassim et al., 2013; Yerro et al., 2015; Wyser et al., 2020). Among these methods, MPM has proven to be both effective and efficient for simulating large deformation problems with history-dependent materials. Originated from the particle-in-cell (PIC) method, MPM is a hybrid Euler-Lagrangian method that has significant advantages in dealing with large deformation problems (Li et al., 2020; Zhao et al., 2023; Fernández et al., 2023). In MPM, a continuum body is discretized by a group of material points carrying all physical information like displacement, velocity, stress, strain, etc. At each time step, the physical information at particles is interpolated to the background mesh, which is essentially Eulerian mesh, and then the governing equations can be solved on it. Subsequently, the solution is re-interpolated to each material particle for the update of particle physical information. The original background mesh can be used again in the new time step, which can eliminate the mesh distortion problem in Lagrangian method, and the accuracy of large deformation problem simulations can

be guaranteed (Fig. 1). Currently, various coupling MPM formulations have been proposed (i.e. the one-point or two-point schemes (Bandara and Soga, 2015; Jassim et al., 2013), the solid displacement-fluid pressure or solid velocity-fluid velocity formulation (Zhang et al., 2009; Lei et al., 2020)) and have been widely used in two-phase coupling problems and engineering applications (Du et al., 2023; Ceccato et al., 2024; Shen et al., 2024; Zheng et al., 2024a; Yamaguchi et al., 2023; Zheng et al., 2024b; Zhan et al., 2025).

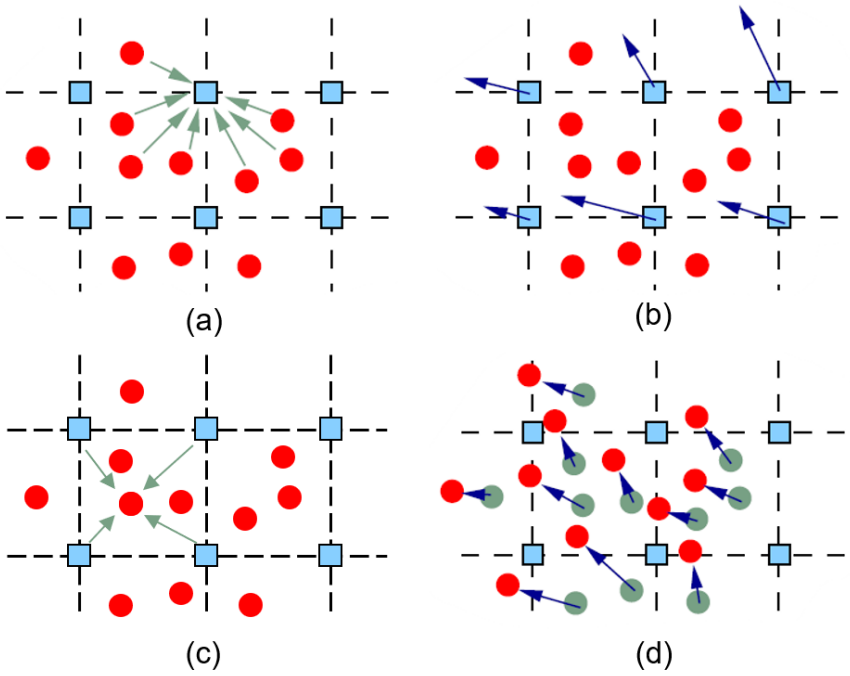

Figure 1. Standard algorithm of MPM: (a) interpolating information from particles to nodes; (b) solving governing equations on nodes; (c) interpolating information from nodes to particles; (d) update particles information.

However, the standard MPM formulation usually employs low-order shape functions within an explicit time integration scheme for simplicity and efficiency, which suffers from the cell-crossing error and the volumetric locking when applied to coupled hydromechanical problems (Li et al., 2024; Sang et al., 2024). The cell-crossing error during particle movement arises from the use of low-order shape functions, which exhibit discontinuous gradients between background mesh elements. To address this issue, higher-order interpolation functions with continuous gradients across elements can be employed, such as the Generalized Interpolation Material Point (GIMP)

77 method (Bardenhagen and Kober, 2004), the B-spline method (De Vaucorbeil et al.,
78 2020) and the Convected Particle Domain Interpolation (CPDI) (Wang et al., 2023b).
79 Due to the low compressibility of pore fluid and limited permeability, the volumetric
80 locking and erroneous strain may occur during simulation, which may not only result
81 in undesired pore pressure oscillation but also render the simulation highly unstable.
82 Various numerical stabilization techniques have been implemented in MPM to solve
83 this issue, including the reduce integration (Bandara and Soga, 2015; Zheng et al.,
84 2021), the B-bar approach (Wang et al., 2018; Tang et al., 2024), the nodal or cell
85 smoothing method (Lei et al., 2020; Wang et al., 2023a), the fractional stepping
86 method (Kularathna et al., 2021; Jassim et al., 2013), the polynomial pressure
87 projection method (Zhao and Choo, 2020), the multi-field variational principle (Liu et
88 al., 2020; Zheng et al., 2021; Tang et al., 2024; Zheng et al., 2022), and coupling with
89 other algorithms (Baumgarten et al., 2021; Li et al., 2024; Tran et al., 2023; Sang et
90 al., 2024). Although these techniques produce results that overcome volumetric
91 locking and reduce pore pressure oscillation, some are conditionally stable, and some
92 require significant modifications of the existing MPM algorithm, leading to additional
93 computation cost and difficulty (Lei et al., 2020; Li et al., 2024). Therefore, their
94 usage should depend on the specific problem at hand. More features and limitations of
95 these techniques can be found in the summary of Li et al. (Li et al., 2024) and Sang et
96 al. (Sang et al., 2024).
97 Here, based on the one-point two-phase MPM scheme (Jassim et al., 2013), we
98 proposes an explicit stabilized two-phase MPM formulation for both static and
99 dynamic analyses of solid-fluid porous media. To avert the volumetric locking and
100 maintain the numerical stability, the stabilized techniques including the strain
101 smoothing method (Mast et al., 2012) and the multi-field variational principle (Chen
102 et al., 2018) have been implemented in the proposed formulation. The strain
103 smoothing method is employed to smooth the volumetric strain rate, and the
104 calculation of the pore pressure increment at particles is based on the multi-field
105 variational principle for accuracy and stability. The spurious pore pressure oscillation
106 can be well mitigated during pore pressure calculation and interpolation. With these

effective and easy-to-implement techniques, the volumetric locking can be significantly eliminated under both static and dynamic conditions. The study is organized as follows. First, the governing equations for solid-fluid two-phase system are briefly introduced in Section 2. The numerical implementation of the proposed formulation and the stabilized techniques are presented in section 3. And then four numerical examples for the verification of the proposed method are performed and analyzed in section 4. Finally, discussion and conclusion are drawn in the last section.

2 Governing equations

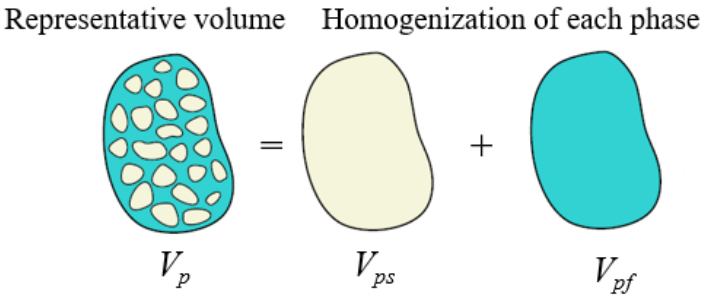

Figure 2. Sketch of material point composition in single-point-two-phase MPM model (Kularathna et al., 2021).

In one-point two-phase MPM formulation, according to the theory of mixture (Baumgarten and Kamrin, 2018), the representative volume (RVE) V_p of a particle material particle is a summation of solid phase volume V_{sp} and fluid phase volume V_{fp}, and each phase (solid, fluid) in the RVE can be characterized by its volume fraction (Fig. 2). The apparent density of each phase is characterized by the intrinsic density with the volume fraction, which reads,

$$\bar{\rho}_s = \varphi\rho_s, \ \bar{\rho}_f = n\rho_f \tag{1}$$

where φ is the solid volume fraction, n is the porosity, ρ_s and ρ_f are the intrinsic density of solid and fluid, respectively; $\bar{\rho}_s$ and $\bar{\rho}_f$ are the apparent density of solid and fluid, respectively.

2.1 Mass conservation equations

The mass conservations in a part of the solid/fluid phase continuum in Lagrangian

description are expressed as,

$$\frac{D^s \bar{\rho}_s}{\mathrm{D}t} + \bar{\rho}_s \nabla \cdot \mathbf{v}_s = 0 \tag{2}$$

$$\frac{D^f \bar{\rho}_f}{Dt} + \bar{\rho}_f \nabla \cdot \mathbf{v}_f = 0 \tag{3}$$

where $\mathbf{v}_s$, $\mathbf{v}_f$ are the velocity of solid and fluid phases in their reference frame, respectively. In microscale, the solid grain is assumed to be incompressible, so ρ_s is constant. However, $\bar{\rho}_s$ will change when the solid phase compacts or dilates due to the deformation of the solid skeleton structure. Therefore, a simple expansion of Eq. (2) using the definition of porosity yields an expression for the change rate of the local measure of porosity,

$$\frac{D^s n}{Dt} = (1-n)\nabla \cdot \mathbf{v}_s \tag{4}$$

In one-point two-phase MPM formulation, all constituents are represented by the same Lagrangian material point in the current configuration. The material time derivative of the fluid phase with respect to the motion of the solid phase is described as follows,

$$\frac{D^f}{Dt} = \frac{D^s}{Dt} + (\mathbf{v}_f - \mathbf{v}_s) \cdot \nabla \tag{5}$$

So, Eq. (3) can be expressed as,

$$\frac{D^s \bar{\rho}_f}{Dt} + (\mathbf{v}_f - \mathbf{v}_s) \cdot \nabla \bar{\rho}_f + \bar{\rho}_f \nabla \cdot \mathbf{v}_f = 0 \tag{6}$$

And Eq. (6) can be further written as,

$$n\frac{D^s \rho_f}{Dt} + \rho_f \frac{D^s n}{Dt} + (\mathbf{v}_f - \mathbf{v}_s) \cdot \nabla n\rho_f + n\rho_f \nabla \cdot \mathbf{v}_f = 0 \tag{7}$$

Assuming the fluid phase is barotropic, density variation in a barotropic fluid obeys the following relationship,

$$\frac{1}{\rho_f}\frac{D^s \rho_f}{Dt} = \frac{1}{K_f}\frac{D^s p_f}{Dt} \tag{8}$$

where K_f is the bulk modulus of fluid, p_f is the pore fluid pressure.

Combining with Eq. (4) and neglecting spatial variations in density and porosity, the pore pressure change rate can be obtained,

$$\frac{D^s p_f}{Dt} = -\frac{K_f}{n}[(1-n)\nabla \cdot \mathbf{v}_s + n\nabla \cdot \mathbf{v}_f] \tag{9}$$

2.2 Momentum conservation equations

The momentum conservation equations for each continuum phase are given as,

$$\bar{\rho}_s \frac{D^s \mathbf{v}_s}{Dt} = \bar{\rho}_s \mathbf{b} - f_b - f_d + \nabla \cdot \boldsymbol{\sigma}_s \tag{10}$$

$$\bar{\rho}_f \frac{D^f \mathbf{v}_f}{Dt} = \bar{\rho}_f \mathbf{b} + f_b + f_d + \nabla \cdot \boldsymbol{\sigma}_f \tag{11}$$

where $\mathbf{b}$ is the body force, which is equal to the gravitational acceleration; f_b and f_d are the buoyant force and inter-phase body force, respectively; $\boldsymbol{\sigma}_s$ and $\boldsymbol{\sigma}_f$ are the solid and fluid stress, respectively. Due to the viscous effects, a flow through porous media results in a drag force, which can be considered as a body force enforced on one phase from the other phase. The classic Darcy's law describes a linear drag force as,

$$f_d = \frac{n\bar{\rho}_f g}{K_s}(\mathbf{v}_s - \mathbf{v}_f) \tag{12}$$

where K_s, in the unit of m/s, is the hydraulic conductivity ($K_s = \rho_f g k/\mu_f$, where k is intrinsic permeability in the unit of m^2 and μ_f is the dynamic viscosity of fluid). This linear relation has been employed in several studies (Zhan et al., 2023; Liu et al., 2017) to model the drag force in saturated porous media when the pore flows are in the laminar flow range with a relatively low Reynolds number. While, the buoyant force, f_b, which yields the form for immiscible mixtures,

$$f_b = p_f \nabla n \tag{13}$$

And the solid phase stress $\boldsymbol{\sigma}_s$ is taken following the effective stress classic form,

$$\boldsymbol{\sigma}_s = \boldsymbol{\sigma}'_s - (1-n) p_f \mathbf{I} \tag{14}$$

where $\mathbf{I}$ is a 3×3 identity matrix, $\boldsymbol{\sigma}'_s$ is the effective solid phase related to the deformation of the solid phase matrix, which excludes the pressurization of the solid phase due to the pressure of the pore fluid. And the fluid phase stress $\boldsymbol{\sigma}_f$ is simplified into an isotropic pressure, $np_f\mathbf{I}$, which is expressed as,

$$\boldsymbol{\sigma}_f = -np_f \mathbf{I} \tag{15}$$

Finally, the momentum equations for solid and fluid phase are given as,

$$\bar{\rho}_s \frac{D^s \mathbf{v}_s}{Dt} = \bar{\rho}_s g - f_d + \nabla \cdot \boldsymbol{\sigma}'_s - (1-n)\nabla p_f \tag{16}$$

$$\bar{\rho}_f \frac{D^f \mathbf{v}_f}{Dt} = \bar{\rho}_f g + f_d - n\nabla p_f \tag{17}$$

With a proper constitutive rule governing the mechanical behavior of the solid effective stress $\boldsymbol{\sigma}'_s$, the equations can fully capture the motion and physical behavior of this two-phase system.

3 Numerical implementations

3.1 Discretized of governing equations

In MPM, the material domain is discretized into Lagrangian material points under Euler background mesh. And the field variables of particles can be interpolated to the background mesh nodes through shape functions. For instance, the displacement and its derivative at particle p is expressed as,

$$u_{pi} = \sum_{I=1}^{N_g} N_{Ip} u_{Ii} \tag{18}$$

$$u_{pi,j} = \sum_{I=1}^{N_g} N_{Ip,j} u_{Ii} \tag{19}$$

where subscripts i and j denote the components of tensor, which follow the Einstein summation convention, and comma between the subscripts indicates partial derivatives; u_{Ii} is the displacement at grid node I, $N_{Ip} = N_I(x_p)$ is the shape function of particle p at grid node I, x_p denotes the coordinates of particle p, $N_{Ip,j}$ is the derivative of shape functions, N_g is total the grid node number. In this study, the GIMP shape function (Bardenhagen and Kober, 2004) and discretization is used to avoid the stress oscillation promoted by the cell-crossing error.

By this way, the momentum equations are discretized in space by means of the Galerkin method considering nodal shape functions. And a discretized form of momentum equation of solid phase Eq. (16) on background mesh node is expressed as,

$$m_{sI} a_{sIi} = f_{sIi}^{int} + f_{sIi}^{ext} \tag{20}$$

where $m_{sI} = \sum_{p=1}^{N_p} N_{Ip} m_{sp}$ is the node mass for solid, in which N_p is total the number of particles and m_{sp} is the particle solid mass; a_{sIi} is the solid acceleration at node, f_{sIi}^{int}

and f_{sIi}^{ext} are the internal and external nodal forces, respectively.

The internal nodal force is expressed as,

$$f_{siI}^{int} = \sum_{p=1}^{N_p}(1-n_p)N_{Ip,j}\,p_{fp}V_p - \sum_{p=1}^{N_p}N_{Ip,j}\sigma'_{spij}V_p \tag{21}$$

where σ'_{spij} is the effective stress of material particle p, p_{fp} is the pore pressure of material particle, n_p is the material particle porosity, V_p is the volume of material particle p.

The external grid nodal force is expressed as,

$$f_{siI}^{ext} = \sum_{p=1}^{N_p}N_{Ip}m_{sp}b_i - \sum_{p=1}^{N_p}N_{Ip}f_d V_p + \int_{\partial\Omega}N_{Ip}\bar{\mathbf{T}}_s dS - \int_{\partial\Omega}(1-n_p)N_{Ip}\bar{\mathbf{P}}dS \tag{22}$$

where $\bar{\mathbf{T}}_s$ and $\bar{\mathbf{P}}$ are the prescribed traction and the prescribed pressure on the boundary $\partial\Omega$, respectively; dS denotes the surface integral that is only non-zero at the boundary $\partial\Omega$.

Likewise, a discretized form of the momentum equation of fluid phase Eq. (17) on the mesh node can be expressed as,

$$m_{fI}a_{fIi} = f_{fIi}^{int} + f_{fIi}^{ext} \tag{23}$$

where $m_{fI} = \sum_{p=1}^{N_p}m_{fp}N_{Ip}$ represents the grid node mass for fluid, in which m_{fp} is the particle fluid mass; $f_{fIi}^{int} = \sum_{p=1}^{N_p}n_p N_{Ip,j}\,p_{fp}V_p$ represents the nodal internal force from pore pressure gradient, $f_{fIi}^{ext} = \sum_{p=1}^{N_p}N_{Ip}m_{sp}b_i + \sum_{p=1}^{N_p}N_{Ip}f_d V_p - \int_{\partial\Omega}n_p N_{Ip}\bar{\mathbf{P}}dS$ denotes the nodal external forces from body force, inter-phase drag force and the boundary prescribed pressure, a_{fIi} is the fluid phase acceleration at mesh node, b_i is the body force vector.

Meanwhile, the strain rate associated with the material point is calculated with its corresponding nodal velocity,

$$\dot{\varepsilon}_{spij} = \sum_{I=1}^{n_g}[N_{Ip,j}v_{si} + (N_{Ip,j}v_{si})^T]/2 \tag{24}$$

$$\dot{\varepsilon}_{fpij} = \sum_{I=1}^{n_g}[N_{Ip,j}v_{fi} + (N_{Ip,j}v_{fi})^T]/2 \tag{25}$$

where v_{si} and v_{fi} are the nodal velocity for the solid phase and fluid phase, respectively; $\dot{\varepsilon}_{spij}$ and $\dot{\varepsilon}_{fpij}$ are the particle strain rate for the solid phase and fluid phase, respectively.

3.2 Numerical stability

As mentioned above, the solid-fluid coupling MPM suffers from the volumetric locking. The stabilized technique is needed for the stability of the simulation. Here, to mitigate the pore pressure oscillation and maintain the numerical stability, the strain smoothing method is used to smooth the particle volumetric strain rate, while the pore pressure increment at particles is calculated based on the multi-field variational principle for the stability, accuracy and smoothness of the results.

3.2.1 Strain smoothing method

The numerically stress/strain smoothing method has been used in the two-phase saturated and unsaturated MPM formulations (Lei et al., 2020; Wang et al., 2023a) and can effectively mitigate the stress oscillation in a simple way. Here, for simplicity and efficiency, a cell-based average approach (Mast et al., 2012) is employed to smooth the particle volumetric strain rate. By doing this, the volumetric strain rate of material points p is replaced by the averaged field value of the cell c which it belongs,

$$\alpha_p = \sum_{p \in c} \alpha_p m_p / \sum_{p \in c} m_p \tag{26}$$

where α_p represents the variables include the volumetric strain rate of solid and fluid, m_p is the mass of material point, representing the solid or fluid mass in different phases.

From the averaged volumetric strain rates $\overline{\varepsilon}_v$, the updated strain rates $\tilde{\dot{\varepsilon}}_{ij}$ is computed by means of,

$$\tilde{\dot{\varepsilon}}_{ij} = \dot{\varepsilon}_d + \overline{\varepsilon}_v \delta_{ij} / 3 \tag{27}$$

where $\dot{\varepsilon}_d$ is the deviatoric strain rate, δ_{ij} is the Kronecker delta. On the basis of the modified strain rates, stresses can be directly computed using the constitutive relation.

3.2.2 The multi-field variational principle

Since the formulation of MPM is analogous to that of the traditional finite element method (FEM), the similar techniques used in FEM for the volumetric locking are also applicable to MPM. The multi-field variational principle is a commonly used anti-locking technique in FEM without using high-order shape functions. In MPM, Chen et al. (Chen et al., 2018) first used the multi-field variational principle to mitigate volumetric-locking and numerical oscillation in weakly compressible problems. And then Liu et al. (Liu et al., 2020) and Tang et al. (Tang et al., 2024) applied this technique in the sing-point two phase unsaturated MPM formulation to mitigate volumetric-locking and carried out the simulation of the Hong Kong Tsui Load landslide and Yanyuan landslide. Zheng et al. (Zheng et al., 2021, 2022) used the multi-field variational principle for the patch recovery of pore pressure increment in the explicit two-point two phase MPM formulation and fully implicit MPM formulation. Based on the multi-field variational principle, the pore pressure field is approximated by expressing the pore pressure increment and the test function as (Chen et al., 2018),

$$\dot{p}_f(\mathbf{x},t) = Q^T(\mathbf{x})a(t) \tag{28}$$

$$\delta\dot{p}_f(\mathbf{x},t) = \delta a^T(t)Q(\mathbf{x}) \tag{29}$$

where $\boldsymbol{Q}$ and $\boldsymbol{a}$ are the polynomial basis function and coefficient vector to be solved. The polynomial basis function can be constant, linear, or quadratic (i.e., $\boldsymbol{Q}$ = [1], [1, x, y, z], or [1, x, y, z, x^2, xy, y^2, yz, z^2, zx], and the corresponding coefficient a = [a_0], [a_0, a_1, a_2, a_3]$^{\mathrm{T}}$, or [a_0, a_1, a_2, a_3, a_4, a_5, a_6, a_7, a_8, a_9, a_{10}]$^{\mathrm{T}}$). Here, in the single-point two-phase MPM formulation, the weak form of the pore pressure rate can be expressed as,

$$\int_\Omega \delta\dot{p}_f(\dot{p}_f + \frac{K_f}{n}[(1-n)\nabla\cdot\mathbf{v}_s + n\nabla\cdot\mathbf{v}_s]d\Omega = 0 \tag{30}$$

And then, the weak form can be changed to,

$$\int_\Omega Q\frac{K_f}{n}[(1-n)\nabla\cdot\mathbf{v}_s + n\nabla\cdot\mathbf{v}_s]d\Omega = -a\int_\Omega QQ^T d\Omega \tag{31}$$

The coefficient can be further expressed as,

$$a = -\mathbf{H}^{-1}\int_\Omega Q\frac{K_w}{n}[(1-n)\nabla\cdot\mathbf{v}_s + n\nabla\cdot\mathbf{v}_s]d\Omega \tag{32}$$

where $\mathbf{H} = \int_\Omega QQ^T d\Omega$. In order to solve the coefficient vector, the node-based method (Mast et al., 2012) is used due to its simplicity and efficiency. Using the node-based method, the node coefficient vector is written as,

$$\mathbf{a}_I = -\mathbf{H}_I^{-1} \sum_{p=1}^{n_p} N_{Ip} Q_p \frac{K_f}{n} [(1-n)\nabla \cdot \mathbf{v}_s + n\nabla \cdot \mathbf{v}_s] V_p \tag{33}$$

where $\mathbf{H}_I = \sum_{p=1}^{n_p} Q_p Q_p^T N_{Ip} V_p$. After solving the coefficient vector for each node, the changing rate of pore pressure can be written as

$$\dot{p}_{fp} = Q_p^T \sum_{I=1}^{n_g} a_I N_{Ip} \tag{34}$$

where $\sum_{I=1}^{n_g} a_I N_{Ip}$ is the node value interpolated to the particle.

3.3 Numerical algorithm

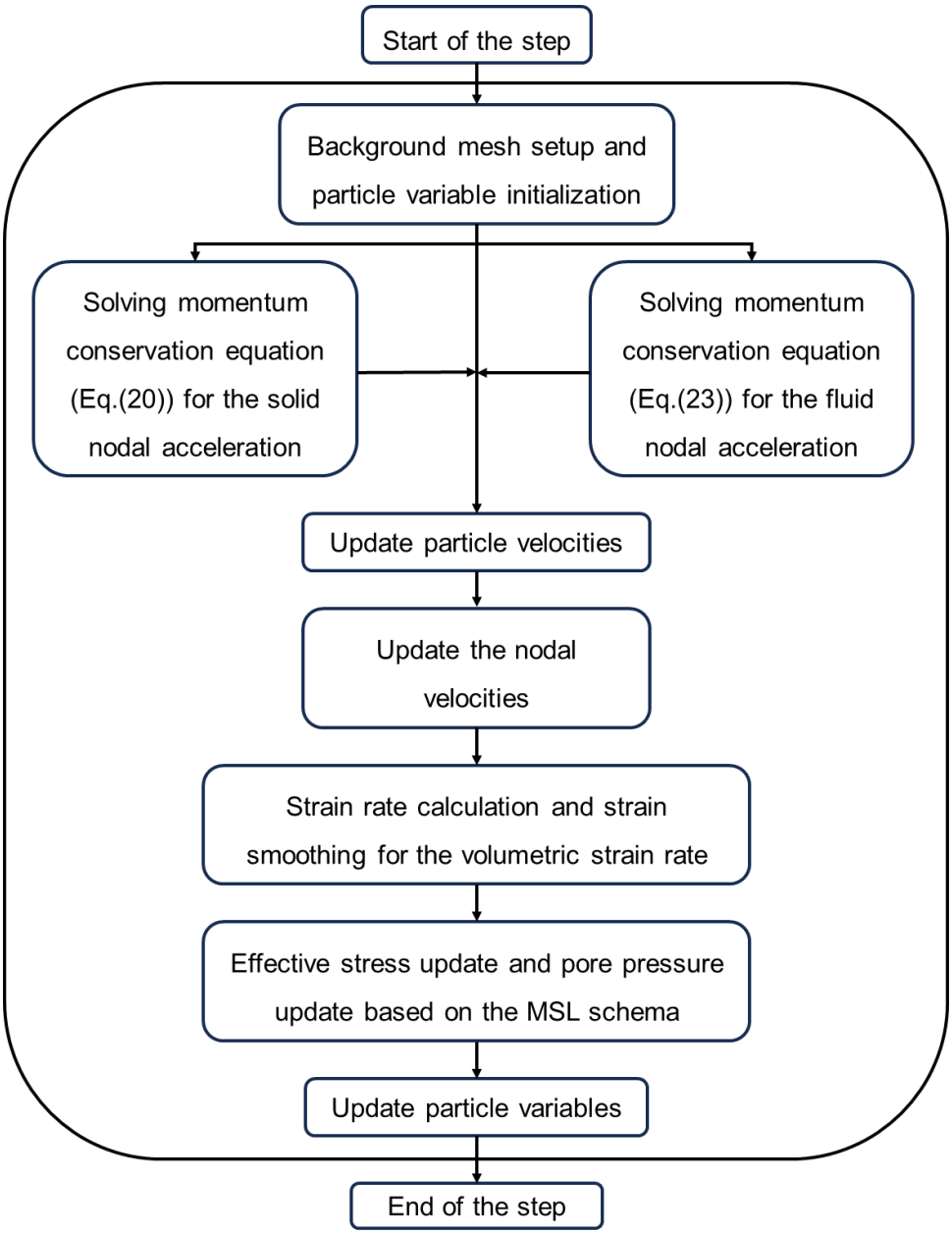

Figure 3. Numerical implementation procedure of the proposed stabilized two phase MPM formulation.

In the proposed formulation, each time step is solved explicitly according to the following sequence of sub-steps (see Fig. 3):

(1) All the variables associated with each material point are initialized first (initial position, stress, pore pressure, etc.);

(2) Interpolate the variables of material points to the nodes of the background mesh using the shape function calculated based on particle locations with respect to the background mesh nodes;

(3) Combined with the correct boundary conditions, the accelerations of each phase on the background mesh node are obtained based on Eq. (20) and (23);

(4) Update the velocity of all material points for both phases using the FLIP scheme (Hammerquist and Nairn, 2017);

(5) Update the nodal velocities for both phases by interpolating velocities back from the material points;

(6) Strain rate increments of solid and fluid phase on particles are calculated, and the cell-based strain smoothing technique expressed in Eq. (26) is applied to smooth the volumetric strain rate;

(7) Update the effective stress based on its constitutive model and the pore pressure based on the multi-field variational principle;

(8) Update the state variables at particles, such as particle volume, porosity and position;

(9) Reset the background mesh for the next step and store all the updated information in material points.

4 Numerical examples

In this section, four numerical examples are conducted to demonstrate the performance of the proposed MPM formulation. First, a one-dimensional consolidation under both small and large conditions is simulated. Subsequently, the two-dimensional consolidation under localized loading and cyclic loading are performed to show its efficacy under external loading. And then, the self-wight consolidation is analyzed to illustrate its capability in simulating undrained and drained conditions, as well as large deformation situation.

4.1 One-dimensional consolidation

The one-dimensional consolidation problem has been frequently studied to verify and assess numerical methods, as it allows a direct comparison with analytical solutions. Here, both small and large deformation conditions are conducted, and the numerical results are compared with their corresponding analytical solutions.

4.1.1 Small deformation

As shown in Fig. 4, a saturated soil column with a width of 0.1 m and a length of 1.0 m is considered for the simulation. An isotropic linear elastic constitutive model is employed, with parameters detailed in Table 1. The background mesh consists of cells sized 0.05 m × 0.05 m, with 4 material points in each mesh element, resulting in a total of 160 material points. Roller normal impermeable boundary is applied to the lateral surfaces, while the bottom is fully fixed and impermeable. The top surface of the column is permeable, allowing fluid to flow out through it. The initial conditions include an excess pore pressure p_0 = 10 kPa and zero effective stress. Not considering gravity, the consolidation process begins by applying a 10 kPa traction to the top material point layer and keeping it constant during the calculation. The time step is set to be 1.0×10^{-5} s with the total simulation time of 2.0 s.

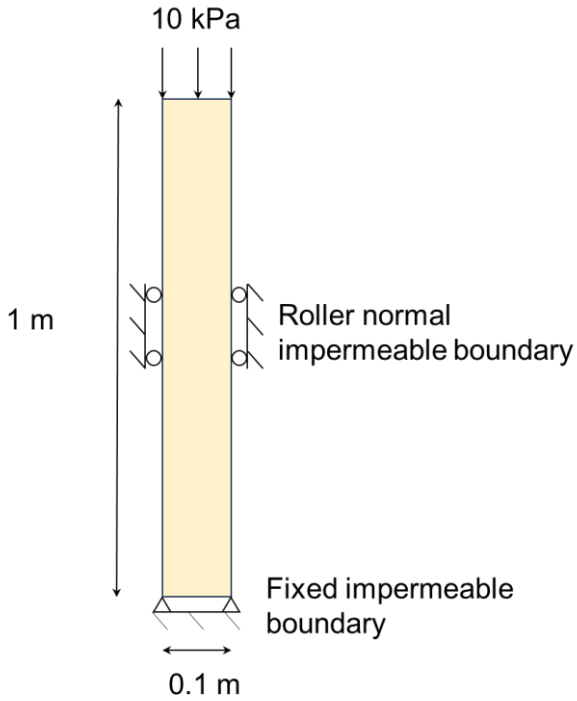

Figure 4. Schematic of the one-dimensional consolidation.

348 **Table 1** Material parameters for the one-dimensional consolidation

Parameter	Value
Solid grain density ρ_s(kg·m^{-3})	2650
Young's modulus E (MPa)	10
Poisson's ratio υ	0.0
Fluid density ρ_w (kg·m^{-3})	1000
Initial porosity n	0.3
Bulk modulus of fluid K_f (Gpa)	2.2
Hydraulic conductivity K_s (m·s^{-1})	0.001

349

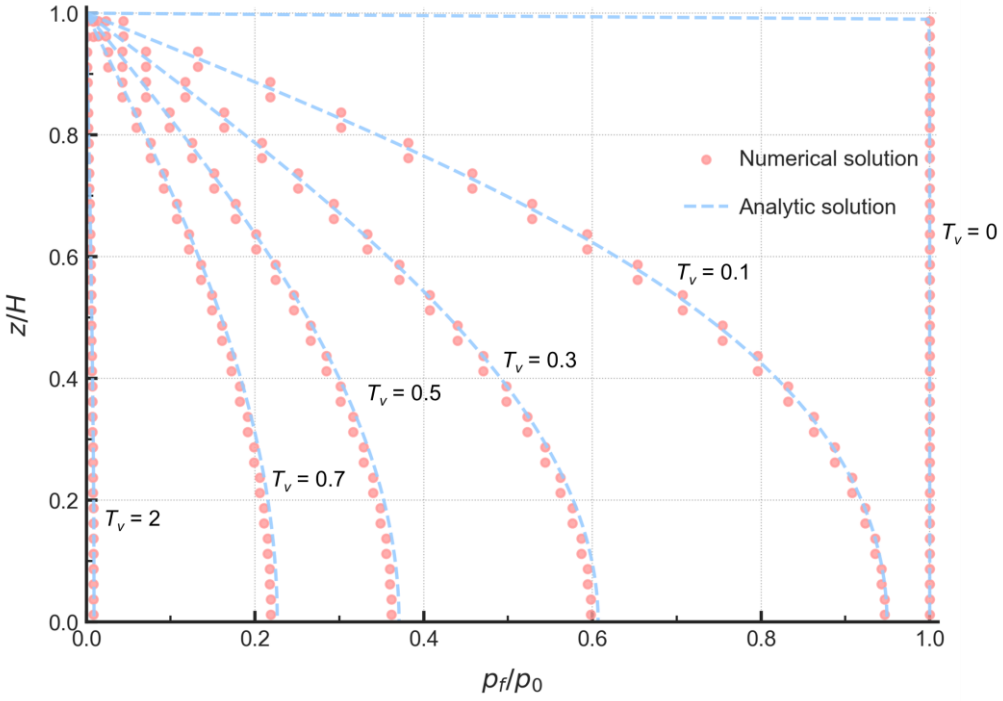

350 **Figure 5.** Comparison of pore pressure profiles from the proposed formulation with
351 Terzaghi's solution.

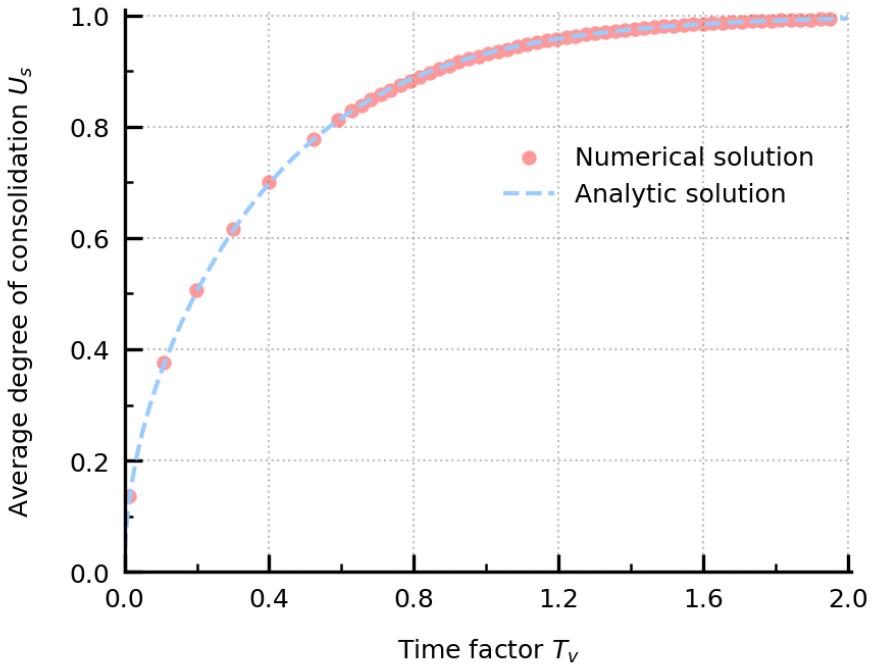

Figure 6. Comparison of the average degree of consolidation from the proposed formulation with Terzaghi's solution.

Under such a constant loading, the deformation of the column is very small and Terzaghi's one-dimensional consolidation theory is applicable. Fig. 5 presents a comparison of the normalized pore pressure distribution at different time factors between the numerical solution and the analytical solution (the time factor $T_v = C_v t / H^2$, where C_v is the coefficient of consolidation and H is the drainage path length). Initially, the pore pressure equals the external load, with the fluid phase undertaking the external loading. Since the external loading is constant, the pore fluid is gradually discharged from the top surface and the pore pressure begins to dissipate progressively from the top. The numerical results show excellent agreement with the analytical solutions, effectively capturing the dissipation process of the excess pore pressure during consolidation. Additionally, the comparison of the average consolidation degree (defined by strain) is presented in Fig. 6, indicating that the numerical results accurately replicate the deformation process as the analytical solution shows.

4.1.2 Large deformation

For the large deformation condition, the same geometry and discretization as in the small deformation case are used. However, a larger top traction (0.2 MPa) is applied, a softer material (E = 1MPa) is considered, and the hydraulic conductivity K_s is adjusted to be 0.0001 m·s^{-1}. Accordingly, the pore pressure is initialized at 0.2 MPa, ensuring that the loading is initially fully carried by the fluid phase. Similar to the small deformation case, the pore pressure will gradually dissipate after applying the constant loading, but now this process will generate considerable vertical deformation. The decrease of the column-length is not negligible, therefore the small-strain Terzaghi's theory is no longer applicable. Based on the large deformation analytical solution (Xie and Leo, 2004), the evolution of pore pressure, top settlement and the average degree of consolidation (defined by strain) can be expressed as,

$$p_f(z,t) = \frac{1}{m_{vl}} \ln[1 + (e^{m_{vl} p_a} - 1) \sum_{m=1}^{\infty} \frac{2}{M} \sin(\frac{Mz}{H}) e^{-M^2 T_v}] \tag{35}$$

$$S_t = H_0 (1 - e^{-m_{vl} p_a})(1 - \sum_{m=1}^{\infty} \frac{2}{M^2} e^{-M^2 T_v}) \tag{36}$$

$$U_s = 1 - \sum_{m=0}^{\infty} \frac{2}{M^2} e^{-M^2 T_v} \tag{37}$$

where m_{vl} = 1 / E is the one-dimensional compressibility, p_a is applied external load, H_0 is the initial depth of the column, z is the distance to the top surface. With the same time step, the total simulation time is 300.0 s.

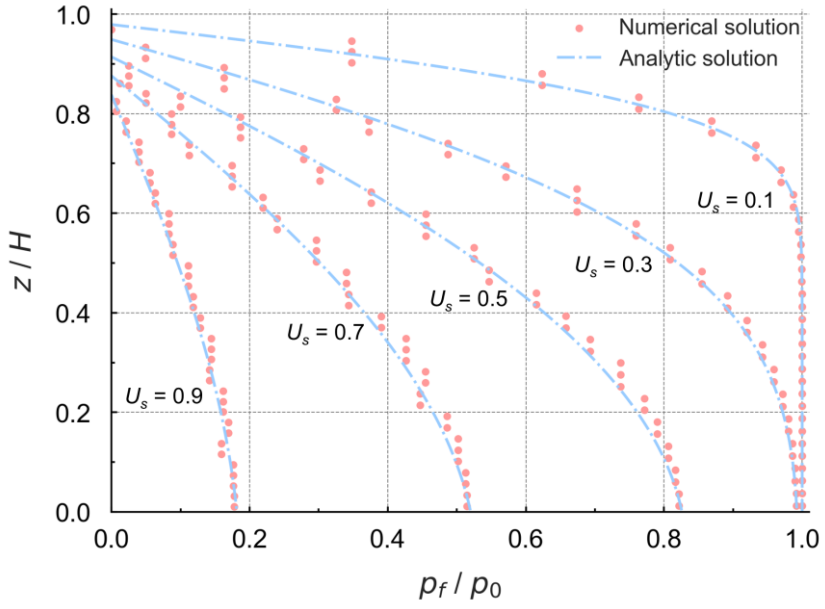

Figure 7. Comparison of pore pressure profiles from the proposed formulation with analytic solution.

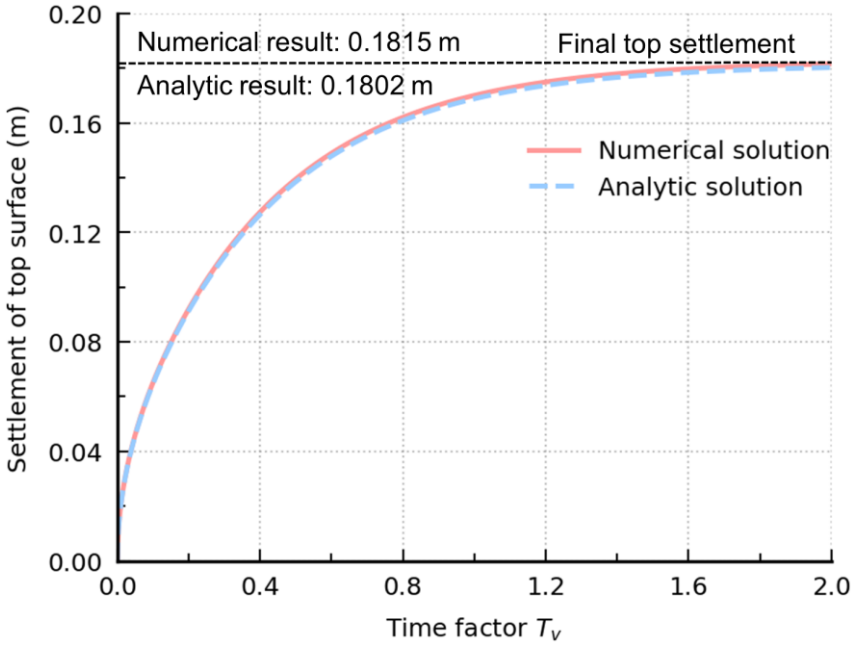

Figure 8. Comparison of the top settlement from the proposed formulation with analytic solution.

Fig. 7 shows the numerical solution of pore pressure evolution along the column height against the results from the analytic solution at different average degrees of consolidation. In the small deformation case, the consolidation coefficient C_v is equal to 1. While for the large deformation case, the consolidation coefficient C_v is very small, so the consolidation is a long process. Hence, the pore pressure dissipation here is much slower than that in the small deformation case. The comparison shows that the numerical results are consistent with the analytic solutions and accurately depict this large deformation consolidation process. The cell average method used in the strain smoothing method will give the same volumetric strain rate for the particles in the same mesh cell, resulting in the same pore pressure distribution in each mesh cell, but the overall trend of this large consolidation process can still be captured. And Fig. 8 shows the evolution of the settlement at the top surface. The numerical result (final top settlement: 0.1815 m) is very close to the analytic result (final top settlement: 0.1802 m). The comparison demonstrates the validation and applicability of the proposed formulation in this two-phase large deformation process.

4.2 Two-dimensional consolidation under localized loading

In this section, a two-dimensional elastic consolidation under a localized loading is simulated, with the geometry and boundary conditions illustrated in Fig. 9. Due to the symmetry of the problem, only half of the domain is modeled. The saturated material domain possesses a dimension of 10.0 m × 10.0 m, while the background mesh consists of cell elements sized 0.05 m × 0.05 m, with 4 material points in each cell element, resulting in 1600 particles. Roller normal impermeable boundary is applied to the lateral surfaces and the bottom, while the top surface is permeable and unconstrained. Initially, a constant local loading of 20.0 kPa, spanning a width of 0.3 m, is applied on the left side of the top surface. Without considering gravity, the initial stress and pore pressure are set to be zero. The isotropic linear elastic constitutive model is used and the material parameters are provided in Table 2. The time step of the simulation is 2.0×10^{-4} s and the total simulation time is 0.1 s. The same simulation has been conducted in the previous studies by semi-implicit MPM scheme (Yuan et al., 2023; Kularathna et al., 2021).

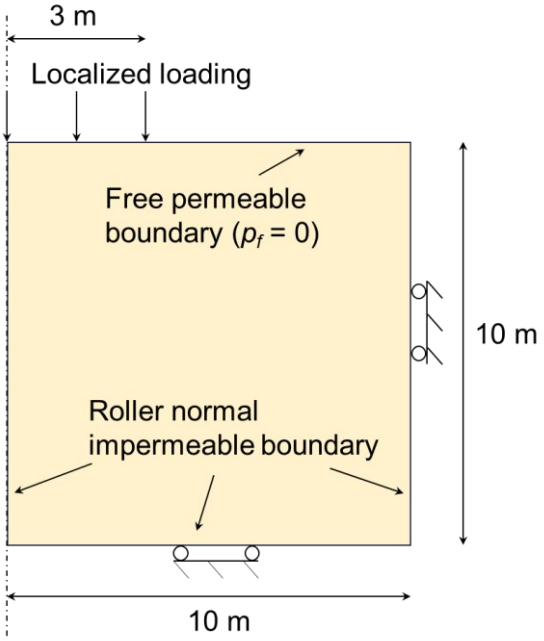

Figure 9. Model setup for the two-dimensional consolidation.

Table 2 Material parameters for the two-dimensional consolidation

Parameter	Value
Solid density ρ_s(kg·m^{-3})	2700
Young's modulus E (MPa)	10
Poisson's ratio υ	0.3
Fluid density ρ_w (kg·m^{-3})	1000
Initial porosity n	0.3
Bulk modulus of fluid K_w (Gpa)	2.2
Hydraulic conductivity K_s (m·s^{-1})	0.0001

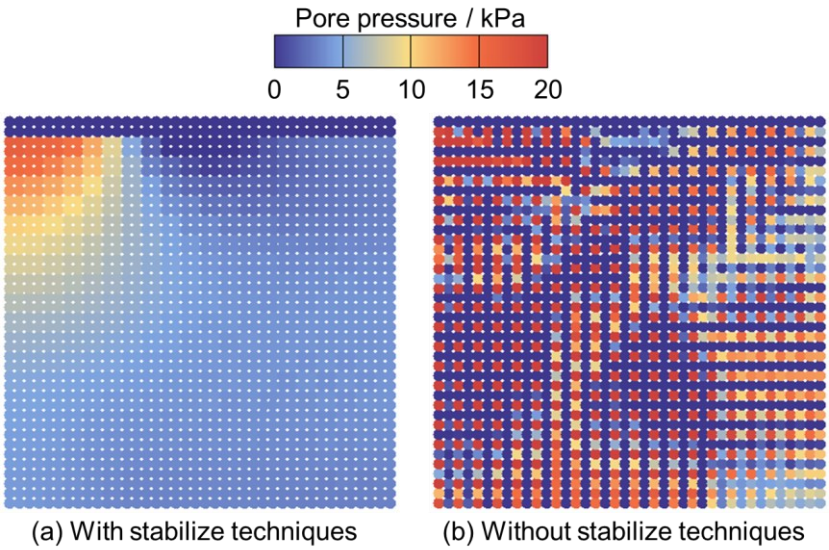

Figure 10. Pore pressure distribution with stabilize techniques and without stabilize techniques at t = 0.1 s.

Fig. 10 illustrates the distribution of pore pressure at time t = 0.1 s, comparing the results obtained with and without stabilized techniques. In Fig. 10b, a spurious pore-pressure field with a checkerboard distribution is observed. In contrast, the result with stabilized techniques shows a smooth excess pore pressure field caused by the external loading (Fig. 10a). It demonstrates that the stabilized techniques can well mitigate pore pressure oscillation in the two phase MPM formulation, offering a stable pressure distribution. And the displacement distribution at t = 0.1 s is shown in Fig. 11. Consistent with the applied local loading, the displacement mainly occurs in the local loading region, indicating that the local loading is undertaken by the upper left corner area. The maximum displacement (6.737 mm) occurs at top left corner, which is

consistent with the result from the semi-implicit MPM formulation (Yuan et al., 2023). Similar results are also obtained using the semi-implicit MPM with artificial compressibility stabilization and fractional–step method (Yuan et al., 2023; Kularathna et al., 2021). The stabilized techniques employed here can yield equivalent results that are free of stress oscillations while accurately preserving the mechanical behavior.

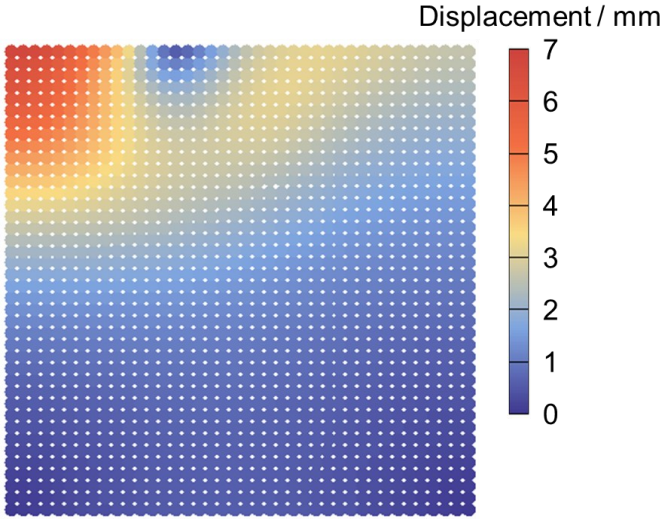

Figure 11. Distribution of displacement field at time t = 0.1 s.

4.3 Cyclic loading test

Inspirited by the lateral cycle loading test (Liang et al., 2023), we conduct a vertical cyclic loading test of a saturated granular material. The model setup is shown in Fig. 12, where the saturated material is placed in a rigid box and subjected to a vertical cyclic loading. The material domain measures 2 m in width and 1 m in height, and is discretized by quadrilateral element with size of 0.05 m × 0.05 m. And there are 4 particles in each element, giving 3200 particles. Both the bottom and laterals are normal impermeable and supported by rollers, and the top is unconstrained and permeable. To apply a cycle loading, the top surface is prescribed by a sinusoidal function periodic load of $40sin5\pi t$ kPa. Table 3 lists the material parameters used for the isotropic linear elastic constitutive model. Before the cyclic stimulation, an equilibrium condition is achieved by a linear gravity loading from 0 to 9.81 m/s^2 within $0 \leq t \leq 0.1$ s, and then the gravity remains constant. And to monitor the cycle

463 loading response, three monitoring points located at the bottle, middle and top of the
464 material domain (A, B, C) are selected (as shown in Fig. 12). The time step is set to be
465 1.0×10^{-5} s, and the simulation is terminated at 2.1 s.

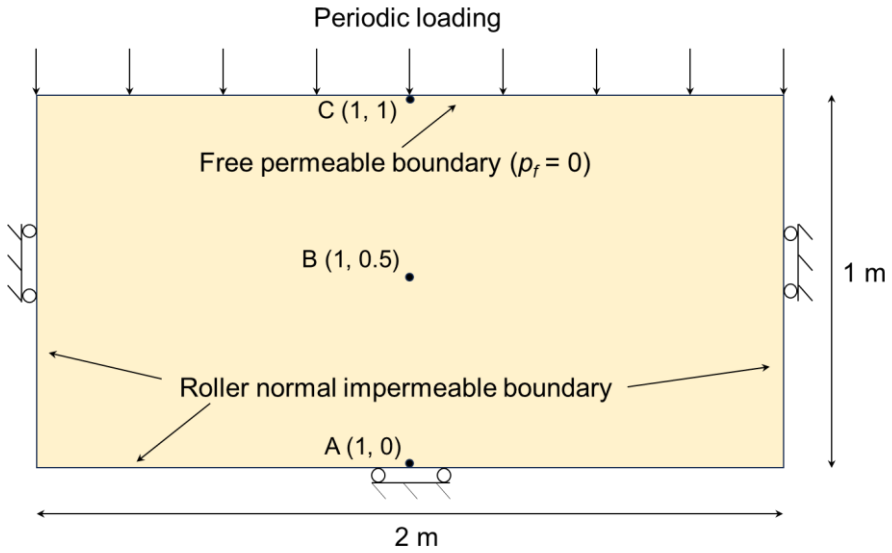

466

467 **Figure 12.** Schematic of cycle loading test.

468 **Table 3** Material parameters for the cycle loading test

Parameter	Value
Solid density ρ_s(kg·m^{-3})	2650
Young's modulus E (MPa)	600
Poisson's ratio υ	0.3
Fluid density ρ_w (kg·m^{-3})	1000
Initial porosity n	0.23
Bulk modulus of fluid K_w (Gpa)	2.2
Hydraulic conductivity K_s (m·s^{-1})	0.001

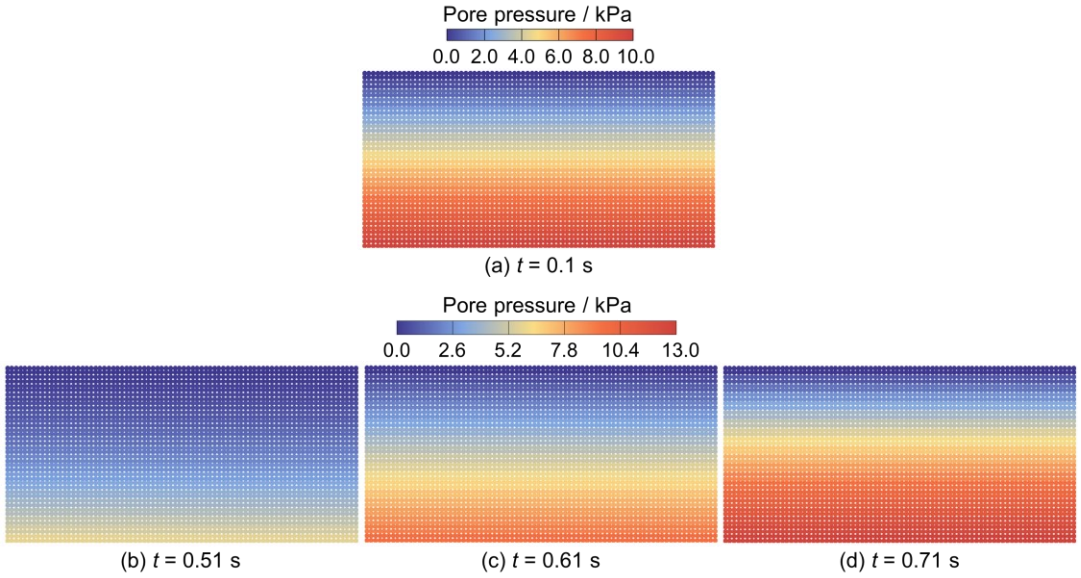

Figure 13. Distribution of pore pressure at $t = 0.1$ s (hydrostatic Pressure), $t = 0.51$ s, $t = 0.61$ s, and $t = 0.71$ s.

Fig. 13 shows the generated pore pressure at four different time instants. After the application of linear gravity loading, an equilibrium condition is achieved, and a hydrostatic pressure field is generated (Fig. 13a). Subsequently, a vertical cyclic loading is applied to the surface. When the material domain is subjected to compressive loading, the pore pressure field increases, whereas under tensile loading, the pore pressure field decreases correspondingly. This vertical cyclic shaking induces an apparent periodic buildup and dissipation of excess pore pressure in the material domain. In Fig. 13b, a clear pore pressure decrease due to tensile loading at $t = 0.51$ s can be seen. As the tensile loading gradually decreases and shifts into compressive loading, the pore pressure will gradually raise up. As a result, the pore pressure field returns to the hydrostatic state at $t = 0.61$ s (Fig. 13c). Subsequently, the compressive loading leads to a further increase in pore pressure. As depicted in Fig. 13d, a significant excess pore pressure field is regenerated. Therefore, the pore pressure in the material domain exhibits periodic variations in response to the cyclic loading.

And to further present the cyclic dynamic response under the applied cyclic loading, the evolution of pore pressure and displacement at the selected monitoring points is presented in Fig. 14. The time history of pore pressure and displacement over time demonstrates this cyclic loading response more quantitatively and vividly. The linear

gravity loading ends at t = 0.1 s, during which the displacement remains very small. After that, the vertical loading will induce a relatively large displacement. Under the sinusoidal periodic loading, the vertical displacement of point B and C exhibits a sinusoidal variation, and the pore pressure at point A and B also changes accordingly. These cyclic responses can be well captured by the proposed stabilized MPM formulation.

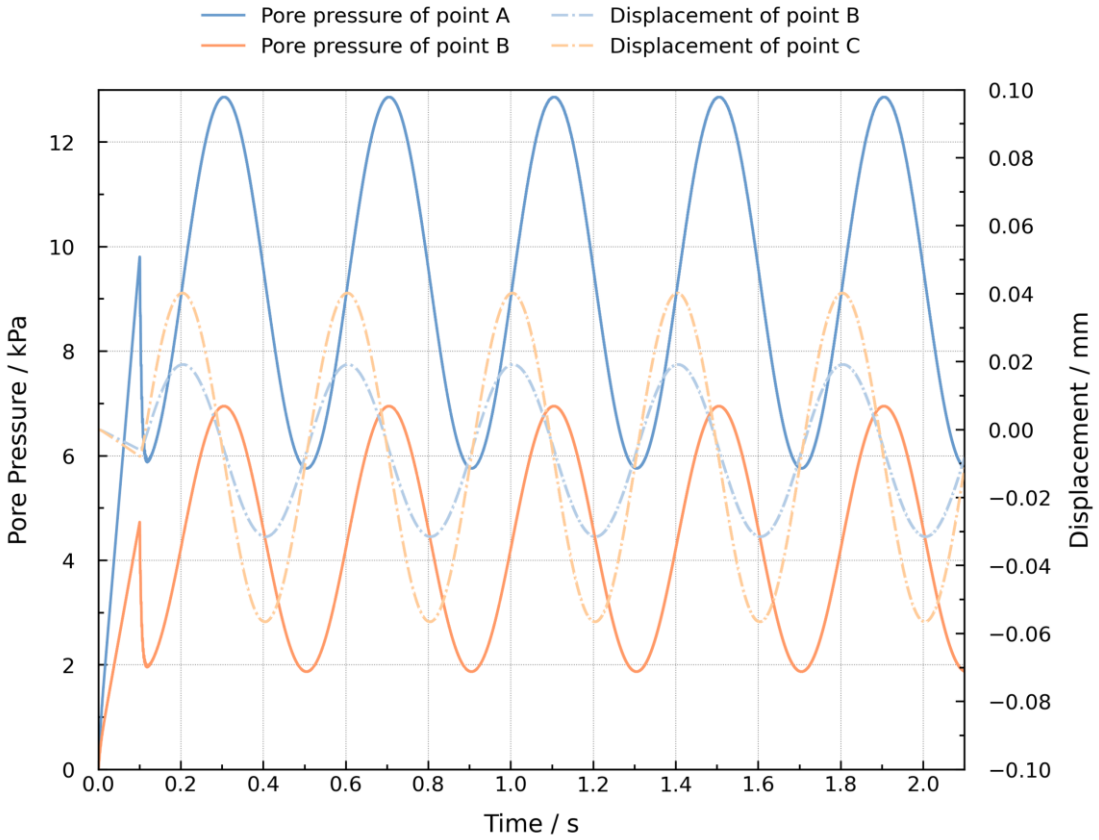

Figure 14. Evolution of pore pressure and displacement at selected points.

4.4 Self-weight consolidation

The large-deformation consolidation of an elastic slumping block under gravity loading is presented in this section (Fig. 15), which is related to the settlement of a very soft soil and has been simulated in previous studies (Zheng et al., 2021, 2022; Sang et al., 2024; Wang et al., 2023a). The simulation focuses on the right half of a symmetric domain with dimensions of 4 m width and 2 m height. The material domain is discretized using quadrilateral element of size 0.125 m× 0.125 m, and 4 particles in each element, giving 1024 particles in total. No external load is applied,

making the consolidation process solely driven by the initial gravitational force at the start of the simulation. The gravity linearly increases from 0 to 9.81 m/s^2 within $0 \leq t \leq 0.1$ s and then remains constant. Both the top and right boundaries are unconstrained and freely draining, while the left and bottom boundaries are normally impermeable and supported by rollers. The gravity will give rise to pore pressure build-up, while the deformation will lead to the dissipation of pore pressure over time. And two points (P_1, P_2) at the bottle and middle are selected to evaluate the consolidation process (as shown in Fig. 15). An isotropic linear elastic constitutive model is used, and the parameters are listed in Table 4. The total simulation time is 0.5, and the simulation is performed with a time step equal to 1.0×10^{-6} s.

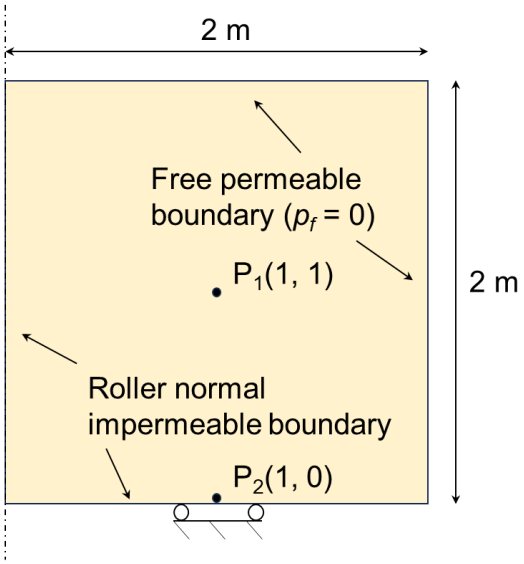

Figure 15. Schematic of the self-weight consolidation

Table 4 Material parameters for the self-weight consolidation

Parameter	Value
Solid density ρ_s(kg·m^{-3})	2650
Young's modulus E (kPa)	100
Poisson's ratio υ	0.3
Fluid density ρ_w (kg·m^{-3})	1000
Initial porosity n	0.4
Bulk modulus of fluid K_w (Gpa)	2.2
Hydraulic conductivity K_s (m·s^{-1})	0.0001

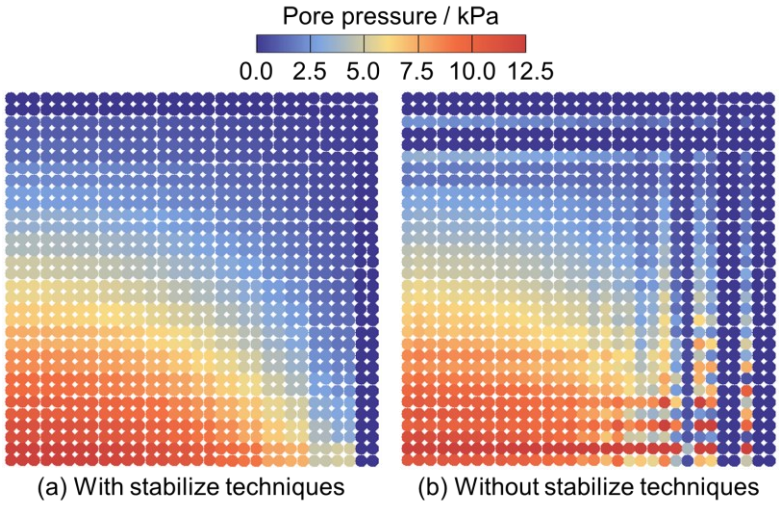

519

520 **Figure 16.** Pore pressures distribution at t = 0.05 s obtained with stabilize techniques

521 and without stabilize techniques.

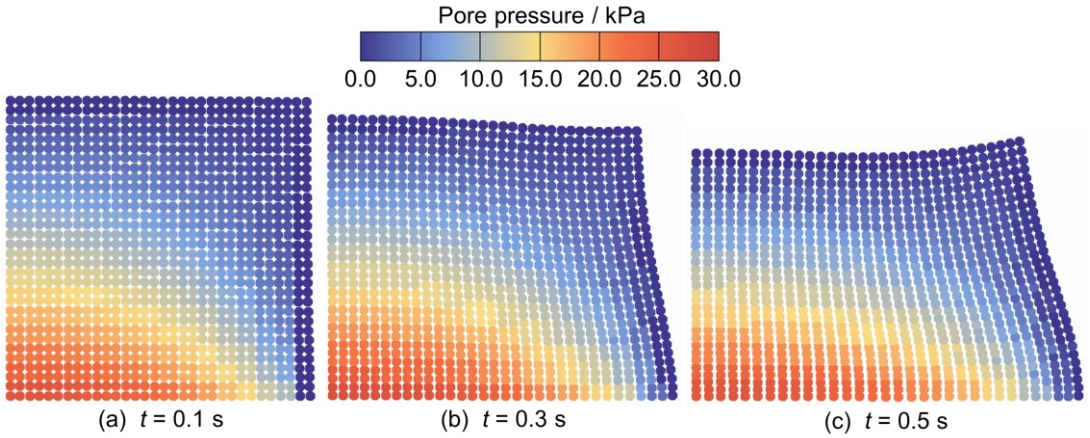

522

523 **Figure 17.** Pore pressures distribution at different times.

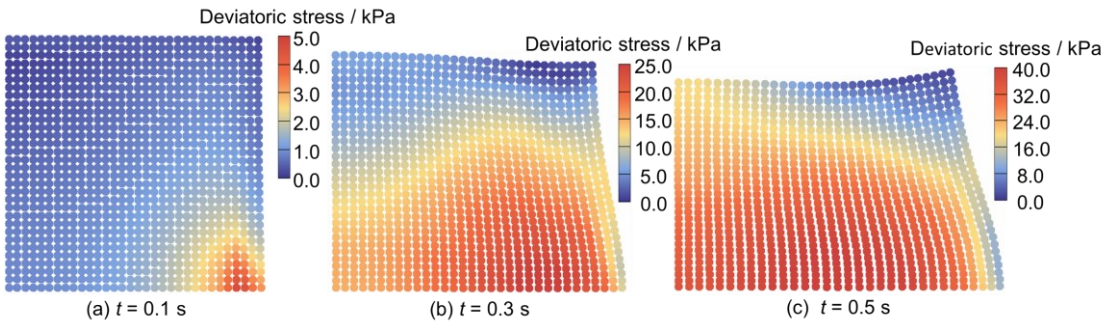

524

525 **Figure 18.** Deviatoric stress distribution at different times.

526 Initially, due to the relatively quick application of gravity loading, the pore fluid

527 cannot be rapidly discharged, and the loading process is carried out under

528 approximately undrained condition. Therefore, the applied gravity loading will induce

529 excess pore pressure at the beginning. Fig. 16 shows pore pressure fields after gravity
530 loading (t = 0.05 s) with stabilized techniques and without stabilized techniques. It
531 can be seen that the result without stabilized techniques suffers from pore pressure
532 oscillations. The stabilized result, in contrast, eliminates spurious oscillations
533 effectively under the stringent undrained condition. Moreover, the distribution of pore
534 pressure and deviatoric stress at three different times (0.1 s, 0.3 s and 0.5 s) are
535 illustrated in Fig. 17 and 18, respectively. Upon the application of linear gravity
536 loading, a pore pressure field develops, gradually decreasing from the bottom left
537 corner upwards, as shown at t = 0.1 s (Fig. 17a). At this stage, the deformation is not
538 large, with a localized region of deviatoric stress distribution observed near the
539 bottom right corner (Fig. 18a). Subsequently, gravity continues to generate pore
540 pressure, and the deviatoric stress gradually increases as deformation progresses. As
541 deformation develops under gravity, the pore pressure first reaches the maximum
542 value and then dissipates because of the deformation and drainage at the boundary.
543 This process can be observed in Fig. 17b, Fig. 18b and Fig. 17c, Fig. 18c. Both pore
544 pressure and deviatoric stress filed change continuously along the large deformation
545 process. The absence of checkerboard oscillations shows the stability of the proposed
546 stabilized formulation in capturing the mechanical behavior of the slumping block
547 during the consolidation process.
548 To further verify the accuracy of the results, the time evolution of the pore pressure at
549 two points (P_1, P_2 in Fig. 15) is shown in Fig. 19, and the results are compared with
550 those of Zheng et al. (Zheng et al., 2022) using implicit stabilized MPM formulation
551 and Sang et al. (Sang et al., 2024) using implicit coupled MPM formulation. During
552 the linear gravity loading, pore pressure increases linearly, followed by non-
553 monotonic dissipation due to the Mandel-Cryer effect. The curves obtained using the
554 proposed stabilized formulation agree well with those of Zheng et al. (Zheng et al.,
555 2022) and Sang et al. (Sang et al., 2024). And the final displacement field (Fig. 20)
556 closely matches the results reported in previous studies (Wang et al., 2023a; Yuan et
557 al., 2023).

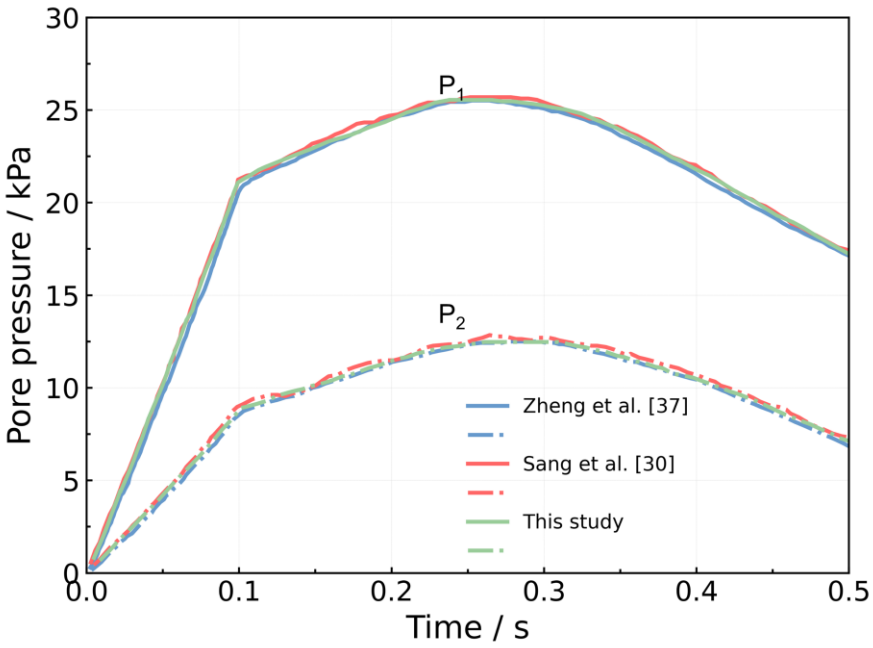

Figure 19. Pore pressures evolution at two selected points.

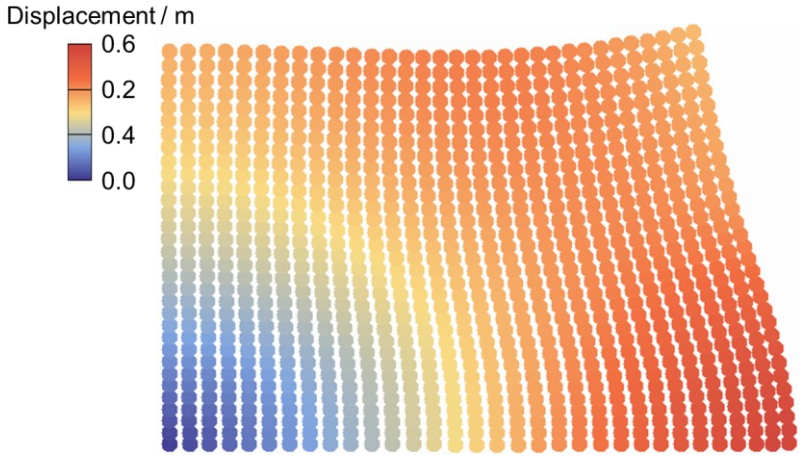

Figure 20. Displacement distribution at 0.5 s.

5 Discussion and conclusion

For the hydromechanical coupling problems in solid-fluid porous media, this study presents an explicit stabilized two-phase material point method by incorporating the strain smoothing method and the multi-field variational principle in the single-point two phase MPM scheme. The proposed model effectively mitigates pore pressure oscillation and maintains numerical stability.

The proposed two-phase MPM was initially validated through one-dimensional consolidation problem under both small and large deformation cases, with the

numerical results showing strong agreement with analytical solutions. It was further assessed through two-dimensional consolidation under localized loading and cyclic loading, demonstrating the formulation's ability in accurately capturing the dynamic response of saturated porous media under external loads. Finally, the self-weight consolidation was analyzed to showcase its efficacy in simulating both undrained and drained conditions, as well as handling large deformation problems. The results aligned closely with analytical solutions and outcomes from other approaches. Particularly, the pore pressure instabilities were greatly mitigated by the stabilized techniques, as clearly validated by the numerical results in terms of pore pressure.

With its effective and easy-to-implement stabilized techniques, the proposed two-phase MPM formulation is well-suited for analyzing a wide range of hydromechanical processes under various undrained, drained, and loading conditions. It offers an effective and reliable approach for simulating both static and dynamic processes in solid-fluid porous media. While the current work is limited to the linear elastic behavior of the solid phase, future efforts will focus on the practice and application involving more complex large deformation problems and advanced constitutive models.

Code and data availability. The model developed in this study is based on the open source MPM code, which is available on Github: https://github.com/xzhang66/MPM3D-F90 (Zhang et al., 2016). The current version of model is available from the project website: https://zenodo.org/records/14899281 under the Creative Commons Attribution licence. The exact version of the model used to produce the results used in this paper is archived on Zenodo (Tang, 2025).

Author Contributions. XT developed the model and wrote the original draft of the paper. WL, SH, LZ and MJ supervised the early stages of the study and provided guidance. HZ, YS and ZH have actively contributed to the formal analysis, as well as the writing and review of the paper. All authors were actively involved in the writing process.

Competing interest. There are no known conflicts of interest associated with this

599 publication.

600 **Financial support.** This work was supported by the National Key Research and
601 Development program of China (Project No. 2022YFF0800604), the Major Program
602 of the National Natural Science Foundation of China (Grant No. 42090051), and the
603 China Scholarship Council (202304910567).

604 **References**

605 Bandara, S. and Soga, K.: Coupling of soil deformation and pore fluid flow using
606 material point method, Comput. Geotech., 63, 199-214,
607 https://doi.org/10.1016/j.compgeo.2014.09.009, 2015.
608 Bandara, S., Ferrari, A., and Laloui, L.: Modelling landslides in unsaturated slopes
609 subjected to rainfall infiltration using material point method, Int. J. Numer. Anal.
610 Methods Geomech., 40, 1358-1380, https://doi.org/ 10.1002/nag.2499, 2016.
611 Bardenhagen, S. G. and Kober, E. M.: The Generalized Interpolation Material Point
612 Method, CMES-Comp Model in Eng. Sci., 5, 477–495,
613 https://doi.org/10.3970/CMES.2004.005.477, 2004.
614 Baumgarten, A. S. and Kamrin, K.: A general fluid–sediment mixture model and
615 constitutive theory validated in many flow regimes, J. Fluid Mech., 861, 721-764,
616 https://doi.org/10.1017/jfm.2018.914, 2018.
617 Baumgarten, A. S., Couchman, B. L. S., and Kamrin, K.: A coupled finite volume and
618 material point method for two-phase simulation of liquid–sediment and gas–
619 sediment flows, Comput. Meth. Appl. Mech. Eng., 384, 113940,
620 https://doi.org/10.1016/j.cma.2021.113940, 2021.
621 Ceccato, F., Yerro, A., and Carluccio, G. D.: Simulating landslides with the material
622 point method: Best practices, potentialities, and challenges, Eng. Geol., 338,
623 107614, https://doi.org/10.1016/j.enggeo.2024.107614, 2024.
624 Chen, F., Li, H., Gao, Y., and Yan, H.: Two-particle method for liquid–solid two-phase
625 mixed flow, Phys. Fluids, 35, 033317, https://doi.org/10.1063/5.0140599, 2023.
626 Chen, Z.-P., Zhang, X., Sze, K. Y., Kan, L., and Qiu, X.-M.: *v-p* material point method
627 for weakly compressible problems, Comput. Fluids, 176, 170-181,

https://doi.org/10.1016/j.compfluid.2018.09.005, 2018.

de Vaucorbeil, A., Nguyen, V. P., and Hutchinson, C. R.: A Total-Lagrangian Material Point Method for solid mechanics problems involving large deformations, Comput. Meth. Appl. Mech. Eng., 360, 112783, https://doi.org/10.1016/j.cma.2019.112783, 2020.

Du, W., Sheng, Q., Fu, X., Chen, J., Wei, P., and Zhou, Y.: Post-failure analysis of landslide blocking river using the two-phase double-point material point method: a case of western Hubei, China, Bull. Eng. Geol. Environ., 82, 98, https://doi.org/10.1007/s10064-023-03122-6, 2023.

Fernández, F., Vargas, E., Muller, A. L., Sousa, R. L., and e Sousa, L. R.: Material point method modeling in 3D of the failure and run-out processes of the Daguangbao landslide, Acta Geotech., 19, 4277-4296, https://doi.org/10.1007/s11440-023-02152-4, 2023.

Guan, X. and Shi, H.: Translational momentum of deformable submarine landslides off a slope, J. Fluid Mech., 960,A23, https://doi.org/10.1017/jfm.2023.177, 2023.

Hammerquist, C. C. and Nairn, J. A.: A new method for material point method particle updates that reduces noise and enhances stability, Comput. Meth. Appl. Mech. Eng., 318, 724-738, https://doi.org/10.1016/j.cma.2017.01.035, 2017.

Jassim, I., Stolle, D., and Vermeer, P.: Two-phase dynamic analysis by material point method, Int. J. Numer. Anal. Methods Geomech., 37, 2502-2522, https://doi.org/10.1002/nag.2146, 2013.

Jerolmack, D. J. and Daniels, K. E.: Viewing Earth's surface as a soft-matter landscape, Nat. Rev. Phys., 1, 716-730, https://doi.org/10.1038/s42254-019-0111-x, 2019.

Jin, Y.-F. and Yin, Z.-Y.: Two-phase PFEM with stable nodal integration for large deformation hydromechanical coupled geotechnical problems, Comput. Meth. Appl. Mech. Eng., 392, 114660, https://doi.org/10.1016/j.cma.2022.114660, 2022.

Kularathna, S., Liang, W., Zhao, T., Chandra, B., Zhao, J., and Soga, K.: A semi-implicit material point method based on fractional-step method for saturated soil, Int. J. Numer. Anal. Methods Geomech., 45, 1405-1436,

https://doi.org/10.1002/nag.3207, 2021.

Lei, X., He, S., and Wu, L.: Stabilized generalized interpolation material point method for coupled hydro-mechanical problems, Comput. Part. Mech., 8, 701-720, https://doi.org/10.1007/s40571-020-00365-y, 2020.

Li, X., Tang, X., Zhao, S., Yan, Q., and Wu, Y.: MPM evaluation of the dynamic runout process of the giant Daguangbao landslide, Landslides, 18, 1509-1518, https://doi.org/10.1007/s10346-020-01569-2, 2020.

Li, Y., Zhang, J.-M., and Wang, R.: An explicit material point and finite volume sequentially coupled method for simulating large deformation problems in saturated soil, Comput. Geotech., 170, 106270, https://doi.org/10.1016/j.compgeo.2024.106270, 2024.

Li, Y., Hu, W., Zhou, L., Fan, Y., McSaveney, M., and Ding, Z.: Influence of soil density on the solid-to-fluid phase transition in flowslide flume experiments, Eng. Geol., 313, 106964, https://doi.org/10.1016/j.enggeo.2022.106964, 2023.

Lian, Y., Bui, H. H., Nguyen, G. D., and Haque, A.: An effective and stabilised (u–p_l) SPH framework for large deformation and failure analysis of saturated porous media, Comput. Meth. Appl. Mech. Eng., 408, 115967, https://doi.org/10.1016/j.cma.2023.115967, 2023.

Liang, W., Zhao, J., Wu, H., and Soga, K.: Multiscale, multiphysics modeling of saturated granular materials in large deformation, Comput. Meth. Appl. Mech. Eng., 405, 115871, https://doi.org/10.1016/j.cma.2022.115871, 2023.

Liu, C., Sun, Q., Jin, F., and Zhou, G. G. D.: A fully coupled hydro-mechanical material point method for saturated dense granular materials, Powder Technol., 314, 110-120, https://doi.org/10.1016/j.powtec.2017.02.022, 2017.

Liu, X., Wang, Y., and Li, D.-Q.: Numerical simulation of the 1995 rainfall-induced Fei Tsui Road landslide in Hong Kong: new insights from hydro-mechanically coupled material point method, Landslides, 17, 2755-2775, https://doi.org/10.1007/s10346-020-01442-2, 2020.

Mast, C. M., Mackenzie-Helnwein, P., Arduino, P., Miller, G. R., and Shin, W.: Mitigating kinematic locking in the material point method, J. Comput. Phys., 231,

5351-5373, https://doi.org/10.1016/j.jcp.2012.04.032, 2012.

Pudasaini, S. P. and Mergili, M.: A Multi-Phase Mass Flow Model, J. Geophys. Res.-Earth Surf., 124, 2920-2942, https://doi.org/10.1029/2019jf005204, 2019.

Sang, Q.-y., Xiong, Y.-l., Zheng, R.-y., Bao, X.-h., Ye, G.-l., and Zhang, F.: An implicit coupled MPM formulation for static and dynamic simulation of saturated soils based on a hybrid method, Comput. Mech., https://doi.org/10.1007/s00466-024-02549-2, 2024.

Shen, W., Peng, J., Qiao, Z., Li, T., Li, P., Sun, X., Chen, Y., and Li, J.: Plowing mechanism of rapid flow-like loess landslides: Insights from MPM modeling, Eng. Geol., 335, 107532, https://doi.org/10.1016/j.enggeo.2024.107532, 2024.

Tang, X., Li, X., and He, S.: A stabilized two-phase material point method for hydromechanically coupled large deformation problems, Bull. Eng. Geol. Environ., 83, 184, https://doi.org/10.1007/s10064-024-03668-z, 2024.

Tang, X.: A stabilized two-phase material point method model, Zenodo, https://doi.org/10.5281/zenodo.14899281, 2025.

Taylor-Noonan, A. M., Bowman, E. T., McArdell, B. W., Kaitna, R., McElwaine, J. N., and Take, W. A.: Influence of pore fluid on grain-scale interactions and mobility of granular flows of differing volume, J. Geophys. Res.-Earth Surf., 127, https://doi.org/10.1029/2022jf006622, 2022.

Tran, Q. A., Grimstad, G., and Ghoreishian Amiri, S. A.: MPMICE: A hybrid MPM-CFD model for simulating coupled problems in porous media. Application to earthquake-induced submarine landslides, Comput. Meth. Appl. Mech. Eng., 125, e7383, https://doi.org/10.1002/nme.7383, 2023.

Wang, B., Vardon, P. J., and Hicks, M. A.: Rainfall-induced slope collapse with coupled material point method, Eng. Geol., 239, 1-12, https://doi.org/10.1016/j.enggeo.2018.02.007, 2018.

Wang, D., Wang, B., Yuan, W., and Liu, L.: Investigation of rainfall intensity on the slope failure process using GPU-accelerated coupled MPM, Comput. Geotech., 163, 105718, https://doi.org/10.1016/j.compgeo.2023.105718, 2023a.

Wang, M., Li, S., Zhou, H., Wang, X., Peng, K., Yuan, C., and Li, J.: An improved

718 convected particle domain interpolation material point method for large
719 deformation geotechnical problems, Int. J. Numer. Anal. Methods Geomech., 125,
720 e7389, https://doi.org/10.1002/nme.7389, 2023b.
721
722 Wyser, E., Alkhimenkov, Y., Jaboyedoff, M., and Podladchikov, Y. Y.: A fast and
723 efficient MATLAB-based MPM solver: fMPMM-solver v1.1, Geosc. Model Dev.,
724 13, 6265-6284, https://doi.org/10.5194/gmd-13-6265-2020, 2020.
725 Xie, K. H. and Leo, C. J.: Analytical solutions of one-dimensional large strain
726 consolidation of saturated and homogeneous clays, Comput. Geotech., 31, 301-314,
727 https://doi.org/10.1016/j.compgeo.2004.02.006, 2004.
728 Yamaguchi, Y., Makinoshima, F., and Oishi, Y.: Simulating the entire rainfall-induced
729 landslide process using the material point method for unsaturated soil with implicit
730 and explicit formulations, Landslides, 20, 1617–1638,
731 https://doi.org/10.1007/s10346-023-02052-4, 2023.
732 Yerro, A., Alonso, E. E., and Pinyol, N. M.: The material point method for unsaturated
733 soils, Géotechnique, 65, 201-217, https://doi.org/10.1680/geot.14.P.163, 2015.
734 Yuan, W., Zheng, H., Zheng, X., Wang, B., and Zhang, W.: An improved semi-implicit
735 material point method for simulating large deformation problems in saturated
736 geomaterials, Comput. Geotech., 161, 105614,
737 https://doi.org/10.1016/j.compgeo.2023.105614, 2023.
738 Yuan, W. H., Zhu, J. X., Liu, K., Zhang, W., Dai, B. B., and Wang, Y.: Dynamic
739 analysis of large deformation problems in saturated porous media by smoothed
740 particle finite element method, Comput. Meth. Appl. Mech. Eng., 392, 114724,
741 https://doi.org/10.1016/j.cma.2022.114724, 2022.
742 Zhan, Z. Q., Zhou, C., Cui, Y. F., and Liu, C. Q.: Initiation and motion of rainfall-
743 induced loose fill slope failure: New insights from the MPM, Eng. Geol., 346,
744 107909, https://doi.org/10.1016/j.enggeo.2025.107909, 2025.
745 Zhan, Z. Q., Zhou, C., Liu, C. Q., and Ng, C. W. W.: Modelling hydro-mechanical
746 coupled behaviour of unsaturated soil with two-phase two-point material point
747 method, Comput. Geotech., 155, 105224,

748 https://doi.org/10.1016/j.compgeo.2022.105224, 2023.
749 Zhang, H. W., Wang, K. P., and Chen, Z.: Material point method for dynamic analysis
750 of saturated porous media under external contact/impact of solid bodies, Comput.
751 Meth. Appl. Mech. Eng., 198, 1456-1472,
752 https://doi.org/10.1016/j.cma.2008.12.006, 2009.
753 Zhang X., Z Chen Z., Liu Y.: The material point method - a continuum-based particle
754 method for extreme loading cases, Academic Press, 2016.
755 Zhao, S., Zhu, L., Liu, W., Li, X., He, S., Scaringi, G., Tang, X., and Liu, Y.:
756 Substratum virtualization in three-dimensional landslide modeling with the material
757 point method, Eng. Geol., 315, 107026,
758 https://doi.org/10.1016/j.enggeo.2023.107026, 2023.
759 Zhao, Y. and Choo, J.: Stabilized material point methods for coupled large
760 deformation and fluid flow in porous materials, Comput. Meth. Appl. Mech. Eng.,
761 362, 112742, https://doi.org/10.1016/j.cma.2019.112742, 2020.
762 Zheng, X., Pisanò, F., Vardon, P. J., and Hicks, M. A.: An explicit stabilised material
763 point method for coupled hydromechanical problems in two-phase porous media,
764 Comput. Geotech., 135, 104112, https://doi.org/10.1016/j.compgeo.2021.104112,
765 2021.
766 Zheng, X., Pisanò, F., Vardon, P. J., and Hicks, M. A.: Fully implicit, stabilised, three-
767 field material point method for dynamic coupled problems, Eng. Comput., 38,
768 5583-5602, https://doi.org/10.1007/s00366-022-01678-7, 2022.
769 Zheng, X., Wang, S., Yang, F., and Yang, J.: Material point method simulation of
770 hydro-mechanical behaviour in two-phase porous geomaterials: A state-of-the-art
771 review, J. Rock Mech. Geotech. Eng., 16, 2341-2350,
772 https://doi.org/10.1016/j.jrmge.2023.05.006, 2024a.
773 Zheng, Y., Li, J., Zheng, X., Guo, N., and Yang, G.: Pre- and post-failure behaviour of
774 a dike after rapid drawdown of river level based on material point method, Comput.
775 Geotech., 170, 106269, https://doi.org/10.1016/j.compgeo.2024.106269, 2024b.